Two-Dimensional Tracking of Heart Wall for Detailed Analysis of Heart Function at High Temporal and Spatial Resolutions

Yasunori Honjo[1]*, Hideyuki Hasegawa[1,2], and Hiroshi Kanai[2,1]

[1]*Graduate School of Biomedical Engineering, Tohoku University, Sendai 980-8579, Japan*
[2]*Graduate School of Engineering, Tohoku University, Sendai 980-8579, Japan*

For noninvasive and quantitative measurements of global two-dimensional (2D) heart wall motion, speckle tracking methods have been developed and applied. These methods overcome the limitation of tissue Doppler imaging (TDI), which is susceptible to aliasing, by directly tracking backscattered echoes by pattern matching techniques, i.e., the cross-correlation or the sum of absolute differences, in real time. In these conventional methods, the frame rate (FR) is limited to about 200 Hz, corresponding to the sampling period of 5 ms. However, myocardial function during the isovolumic contraction period obtained by these conventional speckle tracking methods remains unclear owing to low temporal and spatial resolutions of these methods. Moreover, the accuracy of the speckle tracking method depends on an important parameter, i.e., the size of the correlation kernel. To track backscattered echoes accurately, it is necessary to determine the optimal kernel size. However, the optimal kernel size has not been thoroughly investigated. In this study, correlation kernel size, which determines the tracking accurately, was optimized by evaluating root mean squared (RMS) errors in the lateral and axial displacements of a phantom estimated by speckle tracking methods at high spatial and temporal resolutions. For this purpose, the RF data from the longitudinal-axis cross-sectional view for the interventricular septum (IVS) were acquired on the basis of parallel beam forming (PBF) to improve temporal and spatial resolutions. A wide transmit beam scanned in 7 different directions sparsely and 16 receiving beams were generated for each transmission. The RF data of the phantom and the heart wall were obtained at high spatial (angle intervals of scan lines: 0.375 degrees) and temporal [frame rate (FR): 1020 Hz] resolutions. The determined optimal size of the correlation kernel was 7.9° × 4.8 mm. Estimated displacements of the phantom were in good agreement with the actual displacement at an RMS error of 0.34 mm. Furthermore, the IVS motion during the isovolumic contraction (IC) was analyzed in detail. The speckle tracking method using the optimal kernel size 7.9° × 4.8 mm was applied to multiple points in IVS to estimate 2D displacements during the IC period. In this period, a rapid displacement of IVS at a small amplitude of 1.5 mm, which suggests the expansion of the left ventricle and has not been measured by conventional tracking methods at a low temporal resolution, was detected by 2D tracking. Furthermore, the displacement on the apical side was found to be delayed by 10 ms compared with that on the basal side. These results indicate the potential of this method in the high-accuracy estimation of 2D displacements and detailed analyses of physiological function of the myocardium. © 2010 The Japan Society of Applied Physics

1. Introduction

For noninvasive and quantitative measurement of global two-dimensional (2D) displacements, speckle tracking methods have been developed and applied.[1–3] These methods overcome the limitation of tissue Doppler imaging (TDI),[4–8] which is susceptible to aliasing, by directly tracking backscattered echoes using regional pattern matching techniques, i.e., the cross-correlation function or the sum of the absolute differences, in real time.[9,10] However, the frame rate (FR) in conventional speckle tracking methods is limited to about 200 Hz, corresponding to the sampling period of heart wall motion of 5 ms. In the isovolumic contraction (IC) period, the heart wall moves rapidly during a short period of about 10 ms.[11] Therefore, the detailed analysis of the heart function has been limited owing to a low temporal resolution of conventional speckle tracking methods. The continuous observation of the heart wall motion requires a temporal resolution much shorter than 10 ms.

Wang *et al.* proposed a method for multi-sector ultrasound imaging with retrospective electrocardiogram (ECG) triggering, which achieved a high frame rate of 481 Hz.[12] Alternatively, the required high temporal resolution (FR > 500 Hz) was realized by scanning the heart wall sparsely at the expense of lateral spatial resolution.[13–15] Therefore, the spatial resolution in the measurement of displacement in the lateral direction has been significantly degraded and the speckle tracking method cannot be used with sparse scanning. In this study, the ultrasonic RF data were acquired on the basis of parallel beam forming so that the 2D displacements of the heart wall and the myocardial function

are measured in detail at a high temporal resolution less than 1 ms (corresponding to a frame rate of 1020 Hz) without significant degradation of spatial resolution.

Moreover, the accuracy of the speckle tracking method depends on an important parameter, i.e., the size of the correlation kernel. To track backscattered echoes accurately, it is necessary to determine the optimal kernel size. However, the optimal kernel size has not been thoroughly investigated. Trahey *et al.* reported that blood flow can be measured by tracking echoes from the popliteal vein by normalized correlation with a correlation kernel size of 2.0×1.5 mm².[16] Similarly, Bohs *et al.* accurately determined the velocity of a string phantom, which moves two-dimensionally at velocities up to 2.5 m/s, with a correlation kernel size of 1.0×2.0 mm². The blood flow in the lateral direction was qualitatively imaged in *in vitro* experiments using a correlation kernel size of 0.8×0.8 mm².[17] However, in these studies, correlation kernel size has not been optimized. Therefore, in this study, the optimal kernel size was determined in a phantom experiment and then, the determined optimal kernel size was applied to the *in vivo* measurement of 2D displacements of the heart wall by normalized cross-correlation between RF echoes.

2. Principles

2.1 Acquisition of RF signals at high frame rate

In conventional sector scanning, scan lines are generated by focusing ultrasound to a certain spatial point in both transmission and reception with properly selected delays for the signals applied to and received by transducer elements. As illustrated in Figs. 1(a-1) and 1(a-2), the directions of the transmit and receive beams coincide. In Figs. 1(a-1) and 1(b-1), transmit beams are shown by dashed lines and in
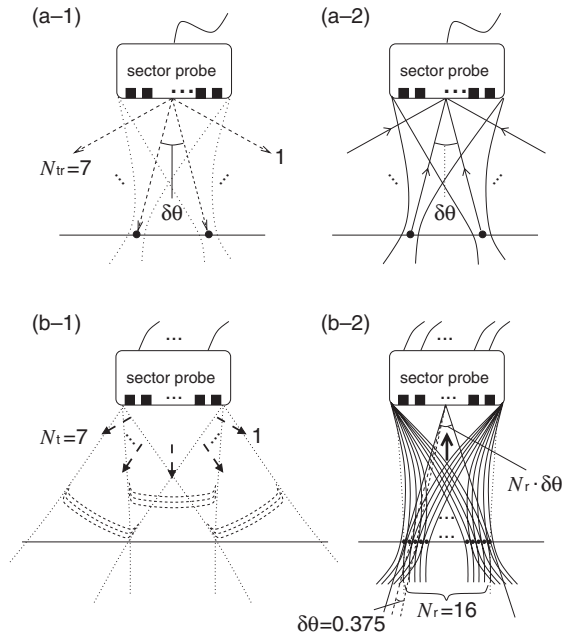
Fig. 1. Transmission and reception of ultrasonic beams. (a) Conventional sector scanning. (b) Parallel beam forming. (1) Transmission. (2) Reception.
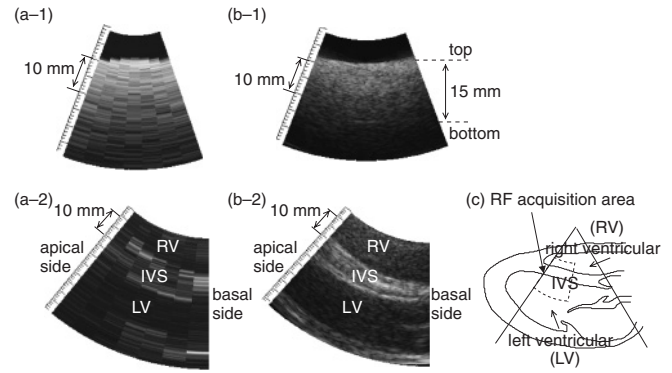

Fig. 2. Comparison of cross-sectional images obtained by sparse scanning (a) with parallel beam forming (b). These are cross-sectional images of a phantom (1) and interventricular septum (IVS) (2). (c) Acquisition area of RF signals in the longitudinal-axis view.

Figs. 1(a-2) and 1(b-2), receive beams are shown by solid lines, respectively. FR in conventional scanning is given by dividing the pulse repetition frequency f_{PRF} by the number N_{tr} of transmit beams, i.e., FR $= f_{PRF}/N_{tr}$. As shown in Figs. 2(a-1) and 2(a-2), on the basis of the conventional sector scan, $N_{tr} = 7$ ultrasonic beams scanned a phantom and a heart wall sparsely at angular intervals of $\delta\theta = 5.6°$ and a high temporal resolution of about $1/600$ s using a 3.75 MHz sector-type probe of ultrasonic diagnostic equipment (Aloka SSD-6500). However, owing to the sparse scanning, the lateral spatial resolution is significantly degraded.

In contrast, parallel beam forming (PBF)[18,19] allows receive beam forming in several directions for each ultrasound transmission. In this study, as shown in Figs. 2(b-1) and 2(b-2), the ultrasonic beams scanned densely on the basis of PBF so that the detailed analysis of the heart wall motion is realized in a wide area at a high temporal resolution of about 1 ms without significant degradation of the lateral spatial resolution. As shown in Fig. 1(b-1), in this study, $N_t = 7$ plane waves were transmitted in seven different directions at angular intervals of 6° at f_{PRF} of 7170 Hz using a 3.75 MHz sector-type probe. In Fig. 1(b-2), for each transmission, $N_r = 16$ receiving beams were generated at angular intervals of $\delta\theta = 0.375°$. The frame rate obtained by PBF is described by FR $= f_{PRF}/N_t = 1020$ Hz. In addition, the total number of received beams was $N_t \times N_r = 112$ and their interval (the lateral angle spacing) was $\delta\theta = 0.375°$. The sampling frequency f_s of the RF signal was 15 MHz. In this study, as described above, a high FR (1020 Hz) acquisition of RF echoes was achieved at a spatial resolution much higher than that of the sparse scan with a wide lateral view of $N_t \times N_r \times \delta\theta = 42°$.

2.2 Evaluation of the normalized cross-correlation function between RF echoes

The algorithm based on the correlation function between

ultrasonic RF echoes is one of the most common methods to estimate the heart wall motion.[3,20–22] In this study, 2D displacements of the heart wall are estimated by employing the normalized cross-correlation function between RF echoes. Figure 3 shows the geometry of speckle tracking based on the regional pattern matching technique using the normalized cross-correlation function (2D tracking). The center of a correlation kernel in the n-th frame is assigned at the lateral and axial coordinates $(\theta, d) \equiv (m, k)$ [point] ($\theta = m \cdot \delta\theta, d = k \cdot \delta d$). The size of the correlation kernel in the lateral direction, W_l, is defined by multiplying the number of beams, $2N_l + 1$ ($\pm N_l$) [points] and the lateral angle spacing $\delta\theta$ (deg/point) [lateral spacing δl (mm/point) of the sampled RF signals] as $W_l = (2N_l + 1) \cdot \delta\theta \equiv (2N_l + 1) \cdot \delta l$. In this study, the lateral angle spacing $\delta\theta$ was set to 0.375° as described in §2.1. The lateral spacing δl (mm/point) at a depth of d was approximately given by

$$\delta l \approx 2d \cdot \sin\left(\frac{\delta\theta}{2}\right). \tag{1}$$

The size of the correlation kernel in the axial direction, W_d, is defined by multiplying the number of sampled RF signals, $2N_d + 1$ ($\pm N_d$) [points], by the axial spacing δd (mm/point) as $W_d = (2N_d + 1) \cdot \delta d$ (mm). The axial spacing δd is defined by the sampling frequency f_s and the sound speed c_0 of the medium as follows:

$$\delta d = \frac{c_0}{2 \cdot f_s}. \tag{2}$$

Speckle size depends on the width of the ultrasonic beam and pulse length.[23,24] Therefore, in this study, the sizes of the correlation kernel in the lateral direction $W_l = (2N_l + 1) \cdot \delta l$ [corresponding to angular width $(2N_l + 1) \cdot \delta\theta$] and that in the axial direction $W_d = (2N_d + 1) \cdot \delta d$ were defined using the widths Δl and Δd at half maxima of the lateral profile of an ultrasonic field and the envelope of an ultrasonic pulse at a depth of 50 mm (focal area), respectively, as shown in Fig. 4. The shape of the correlation kernel was a bivariate normal probability distribution. The variances σ_l^2 (mm) and σ_d^2 (mm) of the normal distribution in the lateral and axial directions were determined as
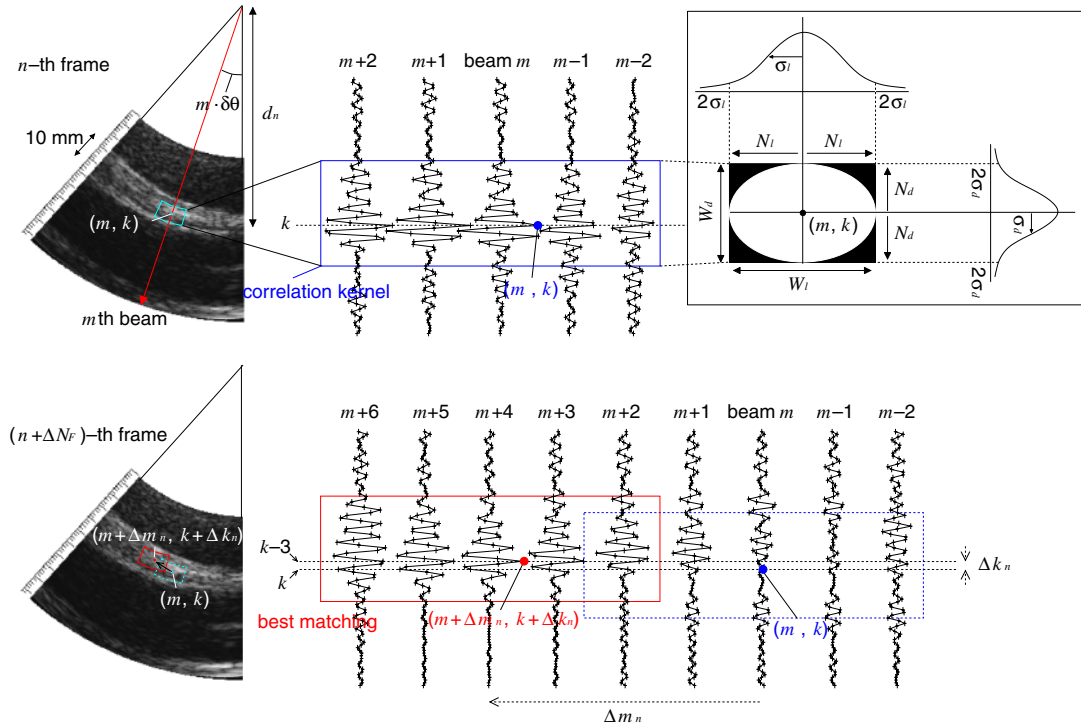
Fig. 3. (Color online) Calculation of normalized cross-correlation function between RF signals in the n-th and $(n + \Delta N_{\mathrm{F}})$-th frames.
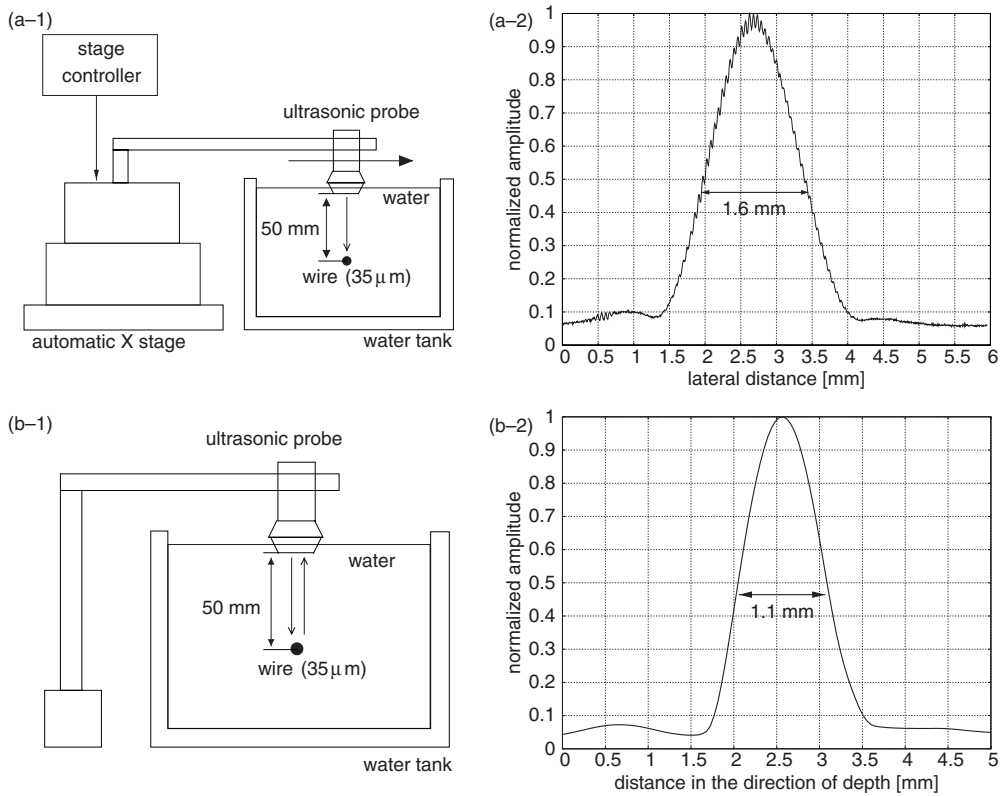

Fig. 4. (a) Schematic image of system for measurement of beam width and measured beam profile. (b) Schematic image of system for measurement of pulse length and measured pulse envelope. The depth d was set at 50 mm (focal area).

$$\sigma_l = \alpha \cdot \Delta l \quad \text{(mm)}, \tag{3}$$

$$\sigma_d = \alpha \cdot \Delta d \quad \text{(mm)}, \tag{4}$$

where α is a constant. The correlation kernel $w(i, j)$ applied to the RF signal $\mathrm{rf}_n(i, j)$ in the n-th frame at i-th lateral point and j-th depth point was defined as follows:

$$w(i, j) = \frac{1}{2\pi\sqrt{\det(\boldsymbol{\Sigma})}} \exp\left[-\frac{1}{2} \mathbf{D}(i, j)^{\mathrm{T}} \boldsymbol{\Sigma}^{-1} \mathbf{D}(i, j) \right], \tag{5}$$

$$\mathbf{D}(i, j) = \begin{pmatrix} i \\ j \end{pmatrix}, \tag{6}$$

$$\mathbf{\Sigma} = \begin{pmatrix} \sigma_l^2 & 0 \\ 0 & \sigma_d^2 \end{pmatrix} = \begin{pmatrix} (\alpha \cdot \Delta l)^2 & 0 \\ 0 & (\alpha \cdot \Delta d)^2 \end{pmatrix}, \quad (7)$$

where $w(i, j)$ is a window function corresponding to the bivariate normal probability distribution, $\mathbf{D}(i, j)$ is a vector from the center of the correlation kernel to the coordinate (i, j) $(i = -N_l, -N_l + 1, \ldots, -1, 0, 1, \ldots, N_l; j = -N_d, -N_d + 1, \ldots, -1, 0, 1, \ldots, N_d)$, and $\mathbf{\Sigma}^{-1}$ is the inverse covariance matrix of the bivariate normal probability distribution $\mathbf{\Sigma}$. In this study, the sizes W_l and W_d of the correlation kernel in the lateral and axial directions were defined by $\pm 2(\sigma_l, \sigma_d) = \pm 2(\alpha \cdot \Delta l, \alpha \cdot \Delta d)$ so that RF signals in the correlation kernel are included in the 95% region of the bivariate normal probability distribution.

The position of the correlation kernel with a size of $(W_l \times W_d) = ((2N_l + 1) \cdot \delta\theta \times (2N_d + 1) \cdot \delta d)$ is assigned manually in the first frame and its central position is tracked in the successive frames. The normalized cross-correlation function $r_{\Theta,D,n}(\Delta m_n, \Delta k_n; \Delta N_F)$ at the lateral shift Δm_n (points) and axial shift Δk_n (points) is calculated from RF signals $\{rf_n(m, k)\}$ and $\{rf_{n+\Delta N_F}(m + \Delta m_n, k + \Delta k_n)\}$ (m: beam number, k: sampled point number of RF signals in the axial direction) in the n-th and $(n + \Delta N_F)$-th frames as follows:

$$\begin{aligned} & r_{\Theta,D,n}(\Delta m_n, \Delta k_n; \Delta N_F) \\ & = \frac{1}{A} \sum_{i=m-N_l}^{m+N_l} \sum_{j=k-N_d}^{k+N_d} \{w(i - m, j - k) \cdot rf_n(i, j) \\ & \quad \times w(i - m, j - k) \cdot rf_{n+\Delta N_F}(i + \Delta m_n, j + \Delta k_n)\}, \quad (8) \end{aligned}$$

$$A = \sigma_{(m,k)} \cdot \sigma_{(m+\Delta m_n, k+\Delta k_n)}, \quad (9)$$

$$\sigma_{(m,k)} = \sqrt{\sum_{i=m-N_l}^{m+N_l} \sum_{j=k-N_d}^{k+N_d} w^2(i - m, j - k) \cdot rf_n^2(i, j)}, \quad (10)$$

where $\sigma_{(m,k)}$ is the standard deviation of the windowed RF signals $\{rf_n(m, k)\}$ in the correlation kernel with a size of $(W_l \times W_d) = ((2N_l + 1) \cdot \delta\theta \times (2N_d + 1) \cdot \delta d)$ and ΔN_F is the frame interval for calculation of correlation. As illustrated in Fig. 3, RF signals in the correlation kernel in the n-th frame are compared with those in the $(n + \Delta N_F)$-th frame. The lateral and axial displacements are determined from the lateral shift $\widehat{\Delta m_n}$ and axial shift $\widehat{\Delta k_n}$, which maximize the normalized cross-correlation function $\{r_{\Theta,D,n}(\Delta m_n, \Delta k_n; \Delta N_F)\}$.

2.3 Reconstructive interpolation

The resolutions in the estimation of the lateral and axial displacements, which are determined from the lateral shift $\widehat{\Delta m_n}$ and axial shift $\widehat{\Delta k_n}$, depend on the lateral angle spacing $\delta\theta$ (deg) [lateral spacing δl (mm)] and the axial spacing δd (sampling interval of the RF signals) of the correlation function. In this study, $\delta\theta$ and δd were set at $0.375°$ and $51.3 \, \mu m$ (sampling frequency $f_s = 15 \, MHz$), respectively. The lateral spacing δl at a typical depth of the interventricular septum (IVS) ($d = 50 \, mm$) is $330 \, \mu m$ and it is much larger than the axial spacing δd of $51.3 \, \mu m$. In this study, the 2D displacements of the heart wall between consecutive frames are expected to be very small because it is measured at a high temporal resolution ΔT of $1 \, ms$. Therefore, the sampling intervals $\delta\theta \, (\equiv \delta l)$ and δd of the coarsely sampled

normalized cross-correlation function are not sufficient for the estimation of 2D displacements.

To overcome this problem, the above normalized cross-correlation function $r_{\Theta,D,n}(\Delta m_n, \Delta k_n; \Delta N_F)$ shown in eq. (8) was interpolated by reconstructive interpolation[20] to improve the accuracy in estimation of the displacement. This method is a space-domain technique based on the signal reconstruction theory using the sinc function, that is, the sampled normalized cross-correlation function $R_{\Theta,D,n}(\Delta m_n', \Delta k_n'; \Delta N_F)$ at an arbitrary lateral shift $\Delta m_n'$ and axial shift $\Delta k_n'$ is given by the following low-pass filtering after increasing spatial sampling frequency:

$$\begin{aligned} & R_{\Theta,D,n}(\Delta m_n', \Delta k_n'; \Delta N_F) \\ & = \sum_{\Delta k_n = -N_d/2}^{N_d/2} \left\{ \left[\sum_{\Delta m_n = N_l/2}^{N_l/2} r_{\Theta,D,n}(\Delta m_n, \Delta k_n; \Delta N_F) \right. \right. \\ & \quad \left. \left. \times \text{sinc}(\Pi_l) \cdot w_h(\Pi_l) \right] \cdot \text{sinc}(\Pi_d) \cdot w_h(\Pi_d) \right\}, \end{aligned}$$

$$\Pi_l = \frac{\Delta m_n' L_l' - \Delta m_n L_l}{L_l} \cdot \pi, \quad (11)$$

$$\Pi_d = \frac{\Delta k_n' L_d' - \Delta k_n L_d}{L_d} \cdot \pi, \quad (12)$$

$$\text{sinc}(\Pi) = \frac{\sin \Pi}{\Pi}, \quad (13)$$

$$w_h(\Pi) = 0.423 - 0.498 \cdot \cos(2\Pi) + 0.0792 \cos(4\Pi), \quad (14)$$

where N_l and N_d are the numbers of the original normalized cross-correlation function in the lateral and axial directions used for interpolation, respectively, L_l, L_d, and L_l', L_d' are the intervals of normalized cross-correlation functions in the lateral and axial directions before and after interpolation, respectively, sinc($\cdot$) is the sinc function, and $w_h(\cdot)$ is the Blackman window.

The lateral and axial average velocities, denoted by $v_l(n; \theta, d)$ and $v_d(n; \theta, d)$, between the n-th and $(n + \Delta N_F)$-th frames are respectively given by the lateral shift $\widehat{\Delta m_n'}$ and axial shift $\widehat{\Delta k_n'}$, determined so that the normalized cross-correlation function in eq. (11) takes the maximum as follows:

$$v_l(n; \theta, d) = \frac{\widehat{\Delta m_n'} \cdot L_l'}{\Delta N_F \cdot \Delta T} \quad \text{(mm/s)}, \quad (15)$$

$$v_d(n; \theta, d) = \frac{\widehat{\Delta k_n'} \cdot L_d'}{\Delta N_F \cdot \Delta T} \quad \text{(mm/s)}, \quad (16)$$

Then, the lateral displacement $x_l(n + 1; \theta, d)$ and the axial displacement $x_d(n + 1; \theta, d)$ at the coordinate (θ, d) in the $(n + 1)$-th frame are estimated as follows:

$$x_l(n + 1; \theta, d) = x_l(n; \theta, d) + v_l(n; \theta, d) \cdot \Delta T \quad \text{(mm)}, \quad (17)$$

$$x_d(n + 1; \theta, d) = x_d(n; \theta, d) + v_d(n; \theta, d) \cdot \Delta T \quad \text{(mm)}. \quad (18)$$

The instantaneous position of the correlation kernel in the $(n + 1)$-th frame is determined by $x_l(n; \theta, d)$ and $x_d(n; \theta, d)$.

3. Determination of the Optimal Size of a Correlation Kernel by Basic Experiment

3.1 Experimental system

Figure 5(a) shows an experimental system. The motion of a phantom was measured to determine the optimum size $(\widehat{W_l} \times \widehat{W_d})$ of the correlation kernel. As shown in Fig. 5(b),
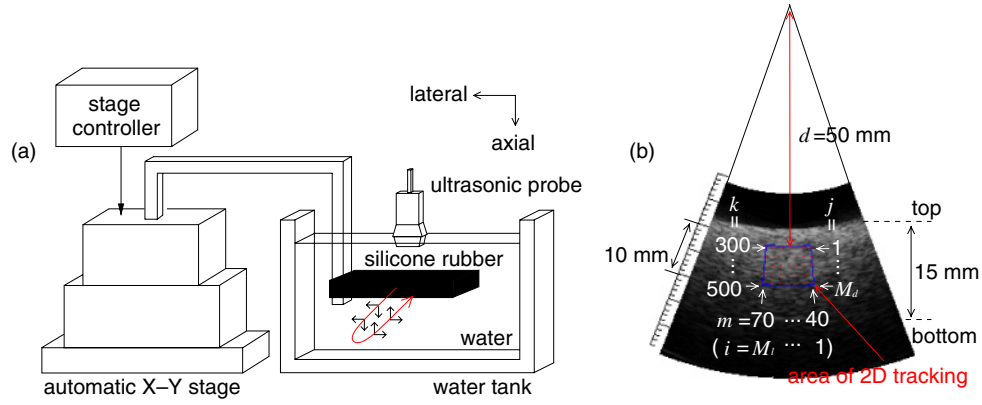
Fig. 5. (Color online) (a) Schematic image of system for basic experiment. (b) Acquired cross-sectional image of silicone rubber. The 2D displacements of the silicone rubber in the area were estimated. The beam number m for the displacement estimation was set at intervals of five beams from 40 to 70. The depth k was set at intervals of 50 points from 300 to 500 from the top of the silicone rubber.

the phantom was made from a silicone rubber (Momentive Performance Materials TSE3503), containing 5% graphite powder by weight to provide sufficient scattering. The phantom was a plate (sound speed c_0: 1000 mm/s) with a thickness of 15 mm. The motion velocity of the silicone rubber was controlled by an automatic X–Y stage. The phantom was moved two-dimensionally. In this study, since the instantaneous rotation component of the regional heart wall motion is negligibly small at a high temporal resolution, this experiment excluded rotational motion. Both the lateral velocity $v_{l0}(n; \theta, d)$ and axial velocity $v_{d0}(n; \theta, d)$ were set at a constant speed of 5 mm/s. However, the velocities $v_{l0}(n; \theta, d)$ and $v_{d0}(n; \theta, d)$ of the silicone rubber in the lateral and axial directions were much lower than the maximum velocities of the actual heart wall motion (about 70 mm/s for both) obtained in separate *in vivo* experiments by the 1D *phased-tracking method*.[11,25,26] Therefore, 2D displacements of silicone rubber between two frames (ΔN_F) in the lateral and axial directions, $x_l(n; \theta, d)$ and $x_d(n; \theta, d)$, were respectively set to be similar to those of the heart wall by increasing the frame interval ΔN_F for calculating correlation function as follows. The frame interval ΔN_F was set at 25 (corresponding 24 ms) in the basic experiment so that the 2D displacements of the silicone rubber between frames ($\Delta N_F \cdot \Delta T$) correspond to the fast motion of the heart wall between two consecutive frames, corresponding to 0.98 ms ($\Delta N_F = 1$) in *in vivo* experiments.

3.2　Determination of the optimal size of the correlation kernel

Estimated displacement depends on the size of the correlation kernel. Therefore, determination of the optimal correlation kernel size is important. When the size of the correlation kernel is set to be small, there may be several regions in the post frame, which have echo patterns similar to those in the correlation kernel in the previous frame. These multiple regions, which have similar echo patterns, introduces misestimation of displacement.[22] On the other hand, when the size of the kernel is set to be large, the echo pattern in the correlation kernel is more unique and the displacement estimation is less susceptible to noise. However, a profile around a peak of the normalized cross-correlation function becomes wider because it is rare that

the echo patterns in two frames coincide, which degrades the accuracy in the estimation and the spatial resolution.[17]

In this study, the sizes W_l and W_d of the correlation kernel in the lateral and axial directions were defined by $\pm 2\sigma_l$ ($= \pm 2\alpha \cdot \Delta l$) and $\pm 2\sigma_d$ ($= \pm 2\alpha \cdot \Delta d$), respectively. To determine the optimal size ($\widehat{W_l} \times \widehat{W_d}$) of the correlation kernel, the 2D displacements estimated using different values of α were examined using the root-mean-squared (RMS) error of the estimated displacement from the actual displacement. The RMS error in the estimated 2D displacements, $\epsilon(\alpha)$, which was evaluated for each value of α, was calculated from the lateral displacement $x_l(\theta, d; \alpha)$ and axial displacement $x_d(\theta, d; \alpha)$ estimated for each position $(\theta, d)_i \equiv (m \cdot \delta\theta, k \cdot \delta d)_i$ [as shown in Fig. 5(b), $i = 1, 2, \ldots, M_l \cdot M_d$ ($m = 40, 45, \ldots, 65, 70$-th beam, $k = 300, 350, \ldots, 450, 500$-th sampling point)] and the actual lateral displacement $x_{l0}(n)$ and axial displacement $x_{d0}(n)$ as follows:

$$\epsilon(\alpha) = \sqrt{\frac{1}{M_l M_d N} \sum_{i=1}^{M_l M_d} \sum_{n=1}^{N} [\Delta x_l(n; i; \alpha)^2 + \Delta x_d(n; i; \alpha)^2]},$$

(19)

$$\Delta x_l(n; i; \alpha) = x_l(n; i; \alpha) - x_{l0}(n), \qquad (20)$$

$$\Delta x_d(n; i; \alpha) = x_d(n; i; \alpha) - x_{d0}(n), \qquad (21)$$

where M_l and M_d are the numbers of measured points in the lateral and axial directions, respectively, and N is the number of averaged frames. In this experiment, as illustrated in Fig. 5(b), the displacements at the positions M ($= M_l \times M_d = 7 \times 5$) = 35 in the area of 2D tracking were measured by normalized cross-correlation functions using different values $\alpha = 0.2$–2.0, corresponding to the kernel sizes $W_l = 1.2$–12.9 mm and $W_d = 0.9$–9.0 mm at a depth of 50 mm. The original sampled normalized cross-correlation function $r_{\Theta,D,n}(\Delta m, \Delta k; \Delta N_F)$ in eq. (8) was interpolated by factors $L'_l / L_l = 60$ in the lateral direction and $L'_d / L_d = 10$ in the axial direction, to obtain the cross-correlation function $R_{\Theta,D,n}(\Delta m'_n, \Delta k'_n; \Delta N_F)$ in eq. (11) with similar resolutions in the lateral and axial directions.

Figure 6 shows the distribution of RMS errors, $\epsilon(\alpha)$, estimated using different values of α of the correlation kernels. When 2D displacements were estimated using a small kernel size, the RMS error was large, as shown in
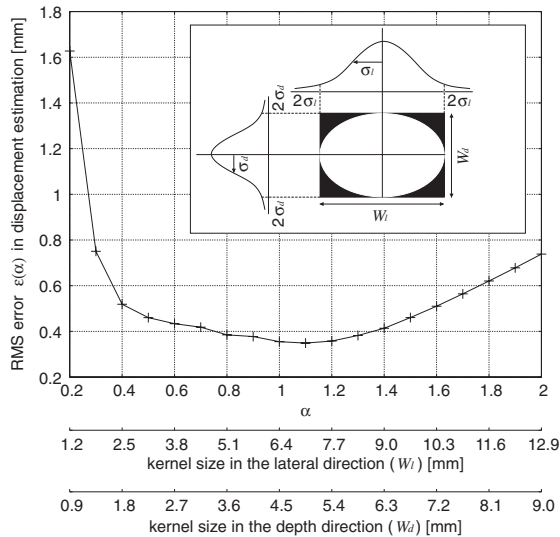
Fig. 6.　Distribution of RMS errors $\epsilon(\alpha)$ for difference sizes of kernels $(W_l \times W_d) = [(1.2-12.9) \times (0.9-9.0)]$ mm.
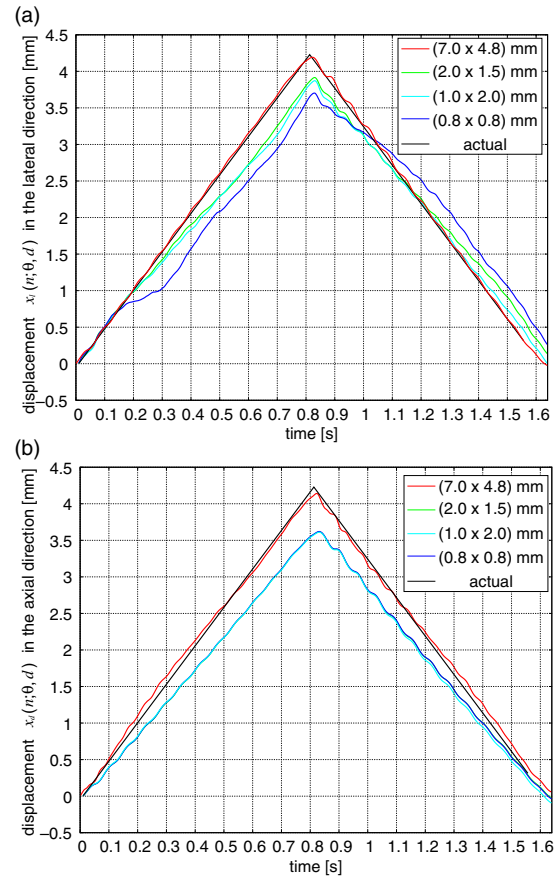

Fig. 7.　(Color online) (a) Estimated displacement $x_l(n; \theta, d)$ and actual displacement $x_{l0}(n)$ in the lateral direction. (b) Estimated displacement $x_d(n; \theta, d)$ and actual displacement $x_{d0}(n)$ in the axial direction. These displacements were estimated using various kernel sizes $(W_l \times W_d)$ of 7.0 × 4.8, 1.0 × 2.0,[16] 2.0 × 1.5, and 0.8 × 0.8 mm².[17] The depth d of each kernel was set as 50 mm at the initial time.

this figure. This result shows that it is impossible to track the 2D displacements accurately using a small and overlarge kernel sizes, such as $(W_l \times W_d) = (1.2 \times 0.9)$ mm $(\alpha = 0.2)$ and $(W_l \times W_d) = (12.9 \times 9.0)$ mm $(\alpha = 2.0)$. On the other hand, when the kernel size was set at $(W_l \times W_d) = (7.0 \times 4.8)$ mm $(\alpha = 1.1)$, the RMS error was minimized to 0.34 mm. This optimal size $(\widehat{W_l} \times \widehat{W_d})$ of the correlation kernel was four times the widths of the ultrasonic beam and the pulse length at a depth of 50 mm (focal area). In this study, the lateral width W_l of sampled points was assumed to be constant because the change in the lateral spacing δl of sampled points in the region of interest (IVS, typical depth and thickness: about 50 and 10 mm) is negligible compared with the ultrasonic beam width Δl. The size of the optimal correlation kernel in the lateral direction, $\widehat{W_l} = 7.0$ mm at the depth $d = 50$ mm, corresponds to 7.9° [the number of the beam in the kernel is $2N_l + 1 = 21$, as shown in eq. (1)].

3.3　Estimation of 2D motion of the silicone rubber using the optimal kernel size

The 2D displacements of the silicone rubber were estimated by the 2D tracking using the optimal kernel size $(\widehat{W_l} \times \widehat{W_d})$ of $(7.9° \times 4.8 \text{ mm}) \equiv (7.0 \times 4.8)$ mm at the depth of $d = 50$ mm. Figures 7(a) and 7(b) show the lateral and axial displacements obtained by the 2D tracking. The displacements estimated for $M = 35$ points in the area of 2D tracking are shown by red lines. The displacements in the lateral and axial directions with the correlation kernel size of $(7.9° \times 4.8 \text{ mm})$ were in good agreement with the actual displacements (black line). On the other hand, the displacements estimated using the previously examined kernel sizes,[16,17] 2.0 × 1.5, 1.0 × 2.0, and 0.8 × 0.8 mm² at the depth $d = 50$ mm in the initial frame, were markedly different from the actual displacement determined by the control of the stepping motor. This result shows that the 2D displacements were estimated accurately by the normalized cross-correlation function with the determined optimal correlation kernel size $(\widehat{W_l} \times \widehat{W_d})$.
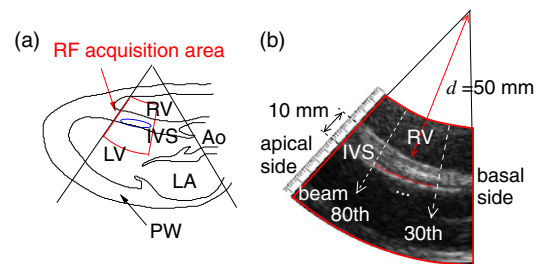

Fig. 8.　(Color online) (a) Acquisition area of RF signals from the longitudinal-axis view. (b) The points employed for estimating 2D displacements are shown by the red points on the cross-sectional image of IVS. The beam numbers were set at 30–80 and the depth was set at 6.0 mm from the chest.

4.　*In vivo* Experimental Results

4.1　Acquisition of RF signals in IVS

Figure 8 shows a typical cross-sectional image (transthoracic parasternal longitudinal-axis view) of the heart obtained from a healthy 22-year-old male. Figure 8(a) shows the RF acquisition area. In the acquisition of RF signals, the ultrasonic beam scanned $N_t \cdot N_r = 112$ different directions densely to maintain a high spatial resolution. The frame rate was set at 1020 Hz. As shown in
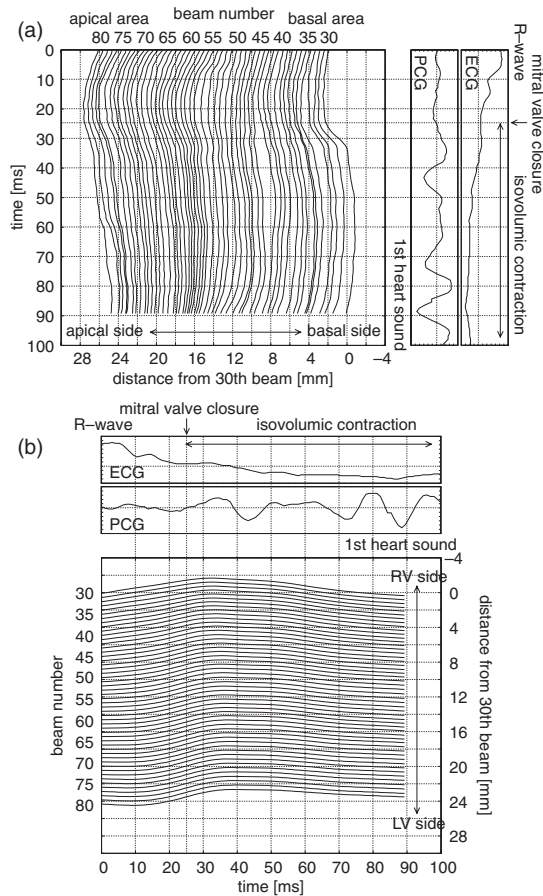
Fig. 9. Displacements of IVS on the left ventricular side in the lateral direction (a) and in the axial direction (b) from R-wave to isovolumic contraction period.

Fig. 10. (Color online) Motion of IVS after R-wave. The cross-sectional images of IVS at every 3 ms (1)–(12). The red lines in these images show the direction and magnitude of instantaneous displacement of IVS. The yellow points in these images show the positions $(\theta, d)_i$ of the *i*-th point of interest, which was set at intervals of five beams from 30 to 80.

Fig. 8(b), the motion of a region in IVS of the left ventricular (LV) side was estimated by 2D tracking. Some features of speckle patterns, such as the size of a speckle, depend on the point spread function produced by the ultrasonic field.[23,24] In this study, as shown in Figs. 2(b-1) and 2(b-2), the RF data were acquired using a 3.75 MHz sector-type probe of ultrasonic diagnostic equipment, which was the same as that used in the basic experiment so that the features of speckle size was not changed. Therefore, the size of a correlation kernel $(\widehat{W_l} \times \widehat{W_d}) = (7.9° \times 4.8\,\text{mm}) \equiv (7.0 \times 4.8)\,\text{mm}$ determined by the basic experiment was also used in the *in vivo* experiment.

4.2 Estimating motions of the interventricular septum from the time of the R-wave to isovolumic contraction period

Figure 9 shows the displacements in the lateral direction $x_l(n; \theta, d)$ and axial direction $x_d(n; \theta, d)$ of IVS on the left ventricular (LV) side plotted as functions of time from the R-wave during isovolumic contraction (IC) period. Figures 10, 11, and 12 show the cross-sectional images of IVS obtained at 3 ms intervals. The red lines in these images show the direction and magnitude of motion of IVS.

As shown in Figs. 9(a) and 10, IVS on the LV side moved to the apical side after the time of the R-wave. This motion of IVS in the apical area was larger than that of IVS in the basal area approximately 20 ms after the R-wave. This suggests that IVS in the basal area was elongated. In
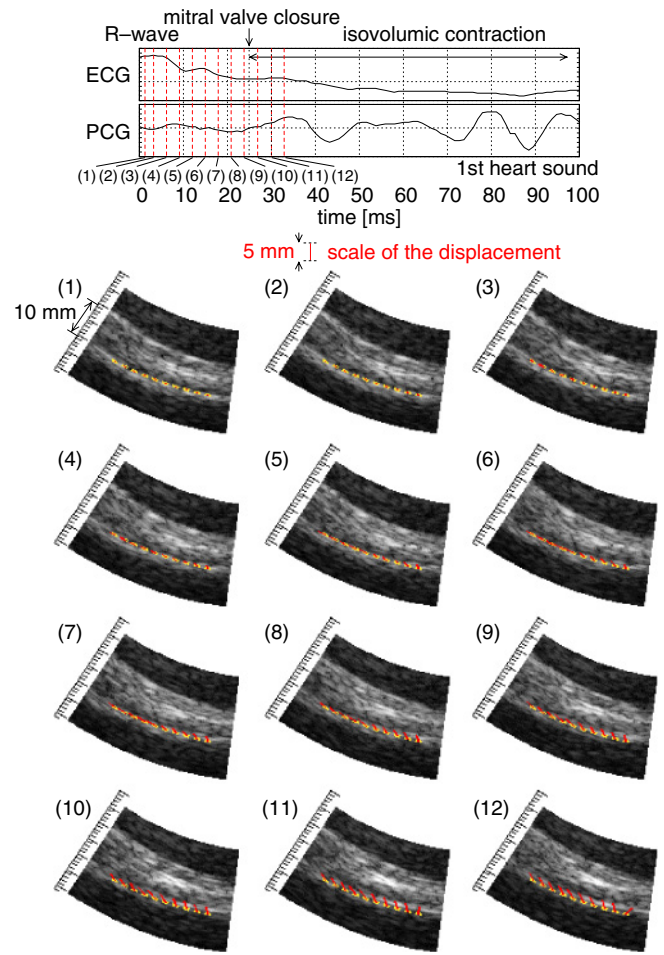
addition, IVS in the basal area moved to the RV side after the time of the R-wave. In contrast, IVS in the apical area moved to the LV side. This is considered to result from an increase in LV pressure owing to contraction of the apical area for the succeeding ejection phase. Figures 9(a) and 10 show that IVS moved from the apical side to the basal side after 10–20 ms from the R-wave. These motions of IVS propagated from the basal area to the apical area, as shown in Figs. 10(5)–(8). At the beginning of the isovolumic phase after the mitral valve closed, IVS in the basal area moved rapidly to the basal side. Moreover, IVS moved from the RV side to the LV side approximately 30 ms from the R-wave. These motions of IVS propagated from the basal area to the apical area, as shown in Fig. 9(b). This suggests that IVS in the basal area was pulled by the motion of the closure of the mitral valve.

As shown in Figs. 9(b) and 11(1)–(5), IVS moved from the RV side to the LV side after 35–45 ms from the R-wave. It is recognized that there is a time delay between the peak of the displacements in the basal area and that in the apical area. The displacement in the apical area was found to be delayed by 10 ms from that in the basal area. Figures 9(b), 11, and 12 show IVS further moved to the LV side after 45 ms. As shown in Figs. 9(a) and 12, IVS in the basal area
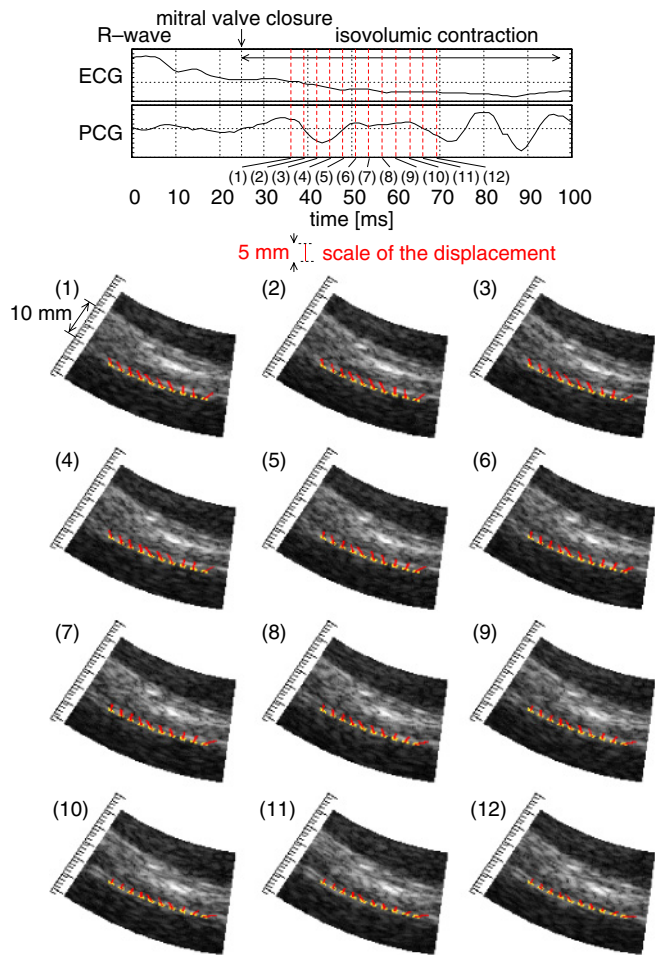
© 2010 The Japan Society of Applied Physics

Fig. 11. (Color online) Motion of IVS from 36 to 69 ms after R-wave. Cross-sectional images of IVS at every 3 ms (1)–(12). The red lines in these images show the direction and magnitude of instantaneous displacement of IVS. The yellow points in these images show the positions $(\theta, d)_i$ of the *i*-th point of interest, which was set at intervals of five beams from 30 to 80.
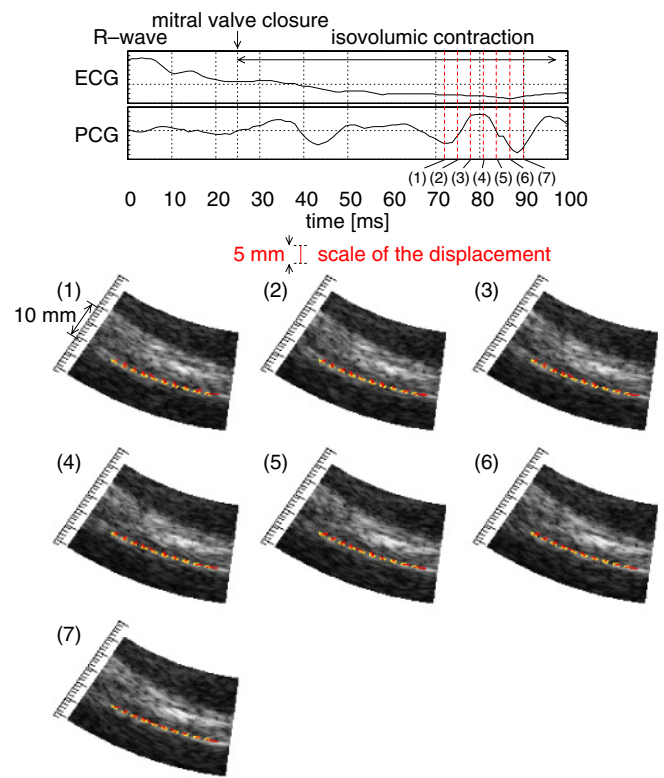

Fig. 12. (Color online) Motion of IVS from 70 to 90 ms after R-wave. Cross-sectional images of IVS at every 3 ms (1)–(7). The red lines in these images show the direction and magnitude of instantaneous displacement of IVS. The yellow points in these images show the positions $(\theta, d)_i$ of the *i*-th point of interest, which was set at intervals of five beams from 30 to 80.

moved to the apical side at the time of 60–80 ms. These motions of the IVS propagated from the basal area to the apical area.

It was found that IVS moved from the apical side to the basal side and RV side during the isovolumic period to increase LV pressure for the succeeding ejection phase. In this study, the displacements in IVS during the IC period could be observed at a high temporal resolution by the proposed method.

5. Conclusions

In this study, an important parameter in 2D displacements estimation was determined to be optimized by RMS errors of the 2D displacements obtained using different sizes of correlation kernels at a high frame rate based on parallel beam forming. The determined optimal size of the correlation kernel was $7.9° \times 4.8$ mm. The estimated displacements of the silicone rubber were in good agreement with the actual displacement. The regional 2D displacements of the heart wall were measured at an extremely high temporal resolution (frame rate about 1020 Hz) without significant increase in the lateral spacing of scan lines (beam interval $\theta_s = 0.375°$). The estimated displacements of IVS were similar to a typical heart wall motion. Furthermore, the IVS motions during isovolumic contraction were analyzed in detail. In this period, a rapid displacement of IVS at a small amplitude of 2.0 mm, which suggested the expansion of the left ventricle and has not been measured by conventional tracking methods at a low temporal resolution, was detected by 2D tracking. Furthermore, the displacement on the apical side was found to be delayed by 10 ms from that on the basal side. Although further investigation to confirm whether the identified relationship between the optimum kernel size and the ultrasonic field can be applied to other depths ($\neq 50$ mm, typical depth of IVS),[27,28] these results indicate the potential of this method in the high-accuracy estimation of 2D displacements and the detailed analyses of the physiological function of the myocardium.

1) L. N. Bohs, B. J. Geiman, M. E. Anderson, S. C. Gebhart, and G. E. Trahey: Ultrasonics **38** (2000) 369.
2) S. Langeland, J. D'hooge, H. Torp, B. Bijnens, and P. Suetens: Ultrasound Med. Biol. **29** (2003) 1177.
3) S. Langeland, J. D'hooge, T. Claessens, P. Claus, P. Verdonck, P. Suetens, G. R. Sutherland, and B. Bijnens: IEEE Trans. Ultrason. Ferroelectr. Freq. Control **51** (2004) 1537.
4) G. R. Sutherland, M. J. Stewart, K. W. Groundstroem, C. M. Moran, A. Fleming, F. J. Guell-Peris, R. A. Riemersma, L. N. Fenn, K. A. Fox, and W. N. McDicken: J. Am. Soc. Echocardiogr. **7** (1994) 441.
5) P. Palka, A. Lange, A. D. Fleming, G. R. Sutherland, L. N. Feen, and W. N. McDicken: J. Am. Soc. Echocardiogr. **8** (1995) 659.
6) K. Miyatake, M. Yamagishi, N. Tanaka, M. Uematsu, N. Yamazaki, Y. Mine, A. Sano, and M. Hirama: J. Am. Coll. Cardiol. **25** (1995) 717.

7) J. Gorcsan III, V. K. Gulati, W. A. Mandarino, and W. E. Katz: Am. Heart J. **131** (1996) 1203.

8) A. Heimdal, A. Støylen, H. Torp, and T. Skjærpe: J. Am. Soc. Echocardiogr. **11** (1998) 1013.

9) T. Numata, H. Hasegawa, H. Kanai, and M. Tanaka: Jpn. J. Appl. Phys. **46** (2007) 4900.

10) H. Yoshikawa, T. Azuma, K. Sasaki, K. Kawabata, and S. Umemura: Jpn. J. Appl. Phys. **46** (2007) 4834.

11) H. Yoshiara, H. Hasegawa, H. Kanai, and M. Tanaka: Jpn. J. Appl. Phys. **46** (2007) 4889.

12) S. Wang, W. Lee, J. Provost, J. Luo, and E. Konofagou: IEEE Trans. Ultrason. Ferroelectr. Freq. Control **55** (2008) 2221.

13) H. Kanai and Y. Koiwa: Ultrasound Med. Biol. **27** (2001) 481.

14) H. Kanai: IEEE Trans. Ultrason. Ferroelectr. Freq. Control **52** (2005) 1931.

15) H. Kanai: Ultrasound Med. Biol. **35** (2009) 382.

16) G. E. Trahey, J. W. Allison, and O. T. von Ramm: IEEE Trans. Biomed. Eng. **34** (1987) 965.

17) L. N. Bohs, B. H. Friemel, B. A. McDermott, and G. E. Trahey: Ultrasound Med. Biol. **19** (1993) 751.

18) D. P. Shattuck, M. D. Weinshenker, S. W. Smith, and O. T. von Ramm: J. Acoust. Soc. Am. **75** (1984) 1273.

19) H. Hasegawa and H. Kanai: IEEE Trans. Ultrason. Ferroelectr. Freq. Control **55** (2008) 2626.

20) I. Cespedes, Y. Huang, J. Ophir, and S. Spratt: Ultrason. Imaging **17** (1995) 142.

21) F. Viola and W. F. Walker: IEEE Trans. Ultrason. Ferroelectr. Freq. Control **50** (2003) 392.

22) D. Rappaport, D. Adam, P. Lysyansky, and S. Riesner: Ultrasound Med. Biol. **32** (2006) 1181.

23) I. Akiyama, A. Hayama, M. Nakajima, S. Yuta, and T. Itoh: Denshi Joho Tsushin Gakkai Ronbunshi D **71** (1988) 733 [in Japanese].

24) R. F. Wagner, S. W. Smith, J. M. Sandrik, and H. Lopez: IEEE Trans. Sonics Ultrason. **30** (1983) 156.

25) H. Kanai, Y. Koiwa, Y. Saito, I. Susukida, and M. Tanaka: Jpn. J. Appl. Phys. **38** (1999) 3403.

26) T. Kinugawa, H. Hasegawa, and H. Kanai: Jpn. J. Appl. Phys. **47** (2008) 4155.

27) G. E. Trahey and S. W. Smith: Ultrason. Imaging **10** (1988) 12.

28) S. W. Smith, G. E. Trahey, S. M. Hubbard, and R. F. Wagner: Ultrason. Imaging **10** (1988) 29.